The International Journal of
Robotics Research
http://ijr.sagepub.com/

Roll and Pitch Motion Analysis of a Biologically Inspired Quadruped Water Runner Robot

Hyun Soo Park, Steven Floyd and Metin Sitti

The International Journal of Robotics Research published online 4 December 2009
DOI: 10.1177/0278364909354391

The International Journal of Robotics Research OnlineFirst, published on December 4, 2009 as doi:10.1177/0278364909354391

Roll and Pitch Motion Analysis of a Biologically Inspired Quadruped Water Runner Robot

Hyun Soo Park
Steven Floyd
Metin Sitti
NanoRobotics Laboratory,
Department of Mechanical Engineering,
Carnegie Mellon University,
5000 Forbes Avenue,
Pittsburgh, PA 15213,
USA
{hyunsoop, srfloyd}@andrew.cmu.edu
sitti@cmu.edu

Abstract

In this paper, the roll and pitch dynamics of a biologically inspired quadruped water runner robot are analyzed, and a stable robot design is proposed and tested. The robot's foot–water interaction force is derived using drag equations. Roll direction instability is attributed to a small roll moment of inertia and large instantaneous roll moments generated by the foot–water interaction forces. Roll dynamics are modeled by approximating the water as a linear spring. Using this model, estimates on the roll moment of inertia that can endure moments generated by water interactions are derived. Instability in the pitch direction is caused by the thrust force the four feet exert on the water. To correct this, a circular tail which can negate the pitch moment around the center of mass is proposed. Both passive and active tail designs which can cope with disturbances are introduced. Based on these analyses, a stable water runner is designed, and built. Experimental high-speed video footage demonstrates the stable roll and pitch motion of the robot. Simulations are used to estimate robustness against disturbances, waves, and leg running frequency variations. It is found that roll motion is more sensitive to disturbances when compared with the pitch direction.

KEY WORDS—biologically inspired robots, quadruped robot, running on water, stability

The International Journal of Robotics Research
Vol. 00, No. 00, Xxxxxxxx 2009, pp. 000–000
DOI: 10.1177/0278364909354391

Figures 2–18, 20–24, 27 appear in color online: http://ijr.sagepub.com

1. Introduction

Small animals and insects utilize diverse techniques to float and locomote upon the surface of water. For example, water striders and spiders, which are very lightweight insects and arachnids, use surface tension (Glasheen and McMahon 1996a; Suter et al. 1994; Song and Sitti 2007). Most heavy animals with masses greater than 1 g that stay at the air–water interface, such as aquatic birds, rely on buoyancy. Only basilisk lizards and shore birds dominantly use the drag forces exerted by the fast motion of their feet on the water, and take advantage of hydrodynamics for locomotion (Bush and Hu 2006; Floyd et al. 2006).

Biologically inspired robots are those robotic systems which imitate some aspects of living organisms. There is considerable literature about aquatic and amphibious robots that use buoyancy and surface tension (Georgiadis 2004; Song et al. 2006; Guo et al. 2003; Boxerbaum et al. 2005; Crespi et al. 2005; Takonobu et al. 2005; Hu et al. 2003). Yet only the water runner robot employs momentum transfer, similar to a basilisk lizard (Floyd et al. 2008; Floyd and Sitti 2008; Floyd et al. 2006). A basilisk lizard's ability to locomote on both land and water using the same legged running mechanism would be a desirable trait for mimicry in robots. Such ability will extend insight into both nature and potential robotics applications. The objective is not to mimic nature, but to understand the principles of operation, and to apply them to accomplish challenging tasks.

Previously, iterative design trials of legged water runner robots have been proposed and built for the purpose of optimizing performance (Floyd et al. 2008; Floyd and Sitti 2008; Floyd et al. 2006). The performance of bipedal and quadrupedal robots were tested and four-bar link lengths for the legs were optimized to produce ideal foot trajectories to generate the lift force (Floyd and Sitti 2008; Floyd et al. 2006). In addition, different types of footpad were discussed for maximizing the lift force in Floyd et al. (2008). As a result of open-water experiments, it was shown that the robot could generate enough overall lift force to support its weight, but the motion was not stable (Floyd and Sitti 2008).

Analyzing and stabilizing the dynamics of the water runner robot is essential for its operation. It was found the previous designs were unstable in both the roll and pitch directions. In the roll direction, the magnitude of the roll moment causes excessively large angular accelerations, often causing the robot to roll to one side and sink. To stabilize the roll motion, the roll moment of inertia must be increased to reduce this acceleration and prevent capsizing in the roll direction.

In the pitch direction, the forward thrust force generated by the legs creates a net moment around the center of mass (COM), causing the front of the water runner robot to tilt upward, and the back end to drag in the water. This change in pose drastically changes the values of lift produced by the feet and causing the robot to sink. A tail which generates a drag force opposite to the running direction is proposed as a device to counteract this moment and stabilize the pitch motion.

For both types of instabilities, the associated forces and torques must be analyzed, and appropriate models generated to understand both destabilization effects, and the dynamic nature of the motion. For simulations, a three-dimensional real-time robot dynamics model based on the original robot CAD model is developed in a virtual environment using a dynamics engine library called *RoboticsLab* (see http://www.rlab.co.kr).

Both experimental and computer models of the water runner robot are described along with the water interaction force modeling in Section 2. By modeling roll motion, a criteria for determining a sufficient moment of inertia for stability is derived and examined in simulation in Section 3. Pitch motion is analyzed and modeled, and the results are used to design both passive and active tails for stability in Section 4. Based on these analyses, an improved design is introduced and tested in Section 5. A computer model of this new design is then analyzed in simulation for robustness to various disturbances in Section 6.

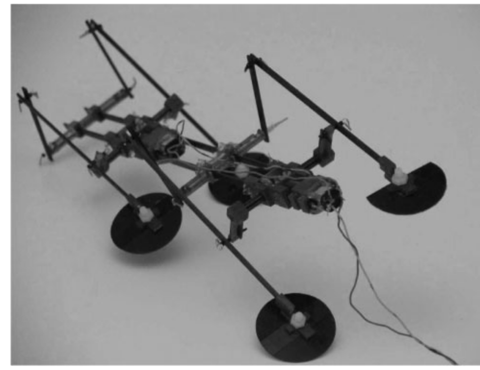

Fig. 1. Photograph of the previous four-legged robot inspired by basilisk lizards. This version can generate sufficient lift force, but it was found to be unstable in the pitch and roll directions. This model described in detail in Floyd and Sitti (2008).

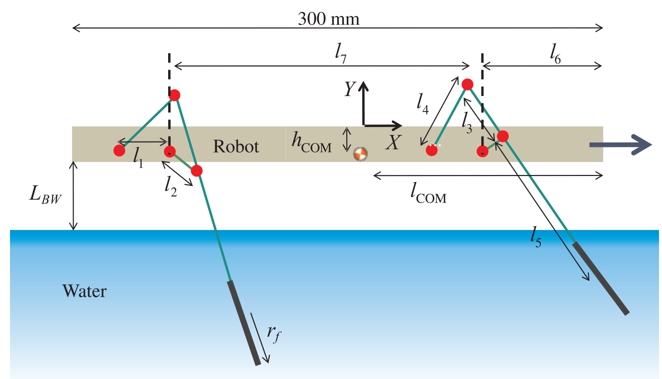

Fig. 2. Schematic of the basic geometry and dimensions of the robot. Lengths for the four-bar mechanism are given in Table 1.

Table 1. Robot Specifications and Dimensions

Robot specification		Link length	
Robot length (mm)	300	l_1 (mm)	61.5
Robot width (mm)	63.2	l_2 (mm)	21.8
Robot mass (g)	61.63	l_3 (mm)	74.8
Moment of inertia		l_4 (mm)	46.8
Roll (kg m^2)	3.99×10^{-5}	l_5 (mm)	62.4
Pitch (kg m^2)	5.31×10^{-4}	l_6 (mm)	53.75
Yaw (kg m^2)	5.32×10^{-4}	l_7 (mm)	173.25
Center of mass and footpad		l (mm)	189.4
l_{COM} (mm)	129	l_t (mm)	100
h_{COM} (mm)	11		
r_f (mm)	20		

2. Water Runner Robot Description and Force Modeling

The first prototype of the water runner robot equipped with off-board battery was discussed thoroughly in Floyd and Sitti (2008) and is shown in Figure 1. Geometric relations are labeled in Figure 2 and referenced in Table 1. This model, which is unstable in both the roll and pitch directions, and the associated parameters are used for initial simulations.

Two footpad designs are examined. One is a simple circular footpad and the other is a directionally compliant footpad which can fold during protraction. When the foot is removed from the water, the normal velocity becomes negative, which causes an undesired pull-off force. This force is exerted over a short period of time, but occurs during the period of maximum

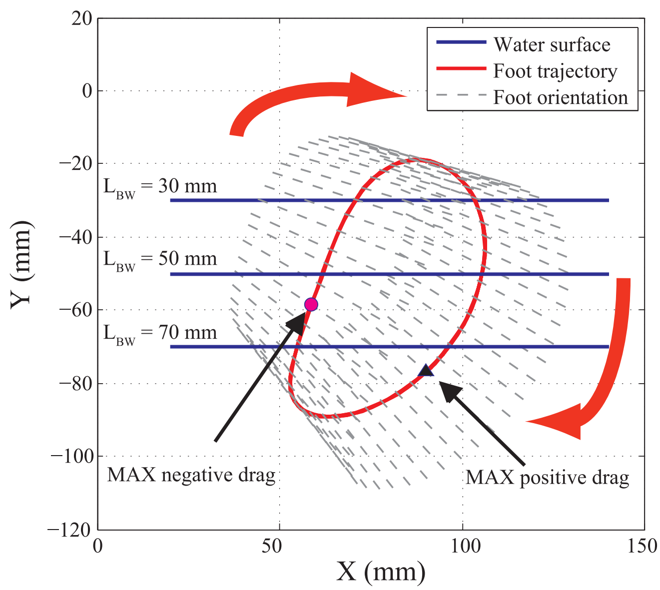

Fig. 3. Simulated trajectory of the foot with footpad orientation shown. The maximum drag occurs when the footpad plane is normal to the foot's velocity. The triangle and circle represent the position of the maximum positive drag and negative drag, respectively.

velocity, as shown in Figure 3, the total momentum change becomes significant. The directionally compliant footpad is used to reduce this effect. When pulling out of the water, two flaps, one on the front and one on the back of the foot can collapse downwards, reducing the area of the footpad normal to the velocity by 69%. This causes a significant improvement in the average lift force. More information on the compliant footpad can be found in Floyd et al. (2008).

2.1. Modeling of The Water Interaction Force

To establish the 3-D modeling in *RoboticsLab*, the interactions between the water runner robot's feet and the water must be appropriately modeled. These models were discussed thoroughly in Floyd and Sitti (2008), and are briefly reviewed here.

There are three phases during one leg rotation cycle: the slap, the stroke, and the protraction phases (Glasheen and McMahon 1996a). Most of the lift force for an adult lizard (those weighing 100 g or more) occurs during the stroke phase (80–90%) (Glasheen and McMahon 1996b,a) and is characterized by the drag force $D(t)$ where

$$D(t) = C_D^*(0.5\rho u^2 S + \rho g h(t) S). \tag{1}$$

Here $C_D^* = 0.707$ is the drag coefficient for a flat, circular disk, ρ is the density of the water, r_f is the radius of foot, $S = \pi r_f^2$ is the area of foot, u is the foot normal velocity, g is the gravitational acceleration, and $h(t)$ is the time-varying depth of the foot below the water's surface. The air cavity created by each step collapses shortly after formation, which puts a lower bound on running frequency of either a basilisk lizard or the water runner robot (Floyd and Sitti 2008; Glasheen and McMahon 1996b).

We assume that, like an adult basilisk lizard, the water runner robot produces lift force primarily from the stroke phase. However, since the robot's footpad cannot become feathered like in the protraction phase of basilisk lizards, the protraction drag cannot be neglected.

To compute the water interaction force and torque, an integral over the submerged area of each foot is performed:

$$f_z = C_D^*\rho \int_0^a \sqrt{r_f^2 - (y - r_f)^2}(v_n|v_n| + 2gh_p)\, dy, \tag{2}$$

$$\tau_x = C_D^*\rho \int_0^a (y - r_f)\sqrt{r_f^2 - (y - r_f)^2} \times (v_n|v_n| + 2gh_p)\, dy, \tag{3}$$

where y is a variable of integration taken along the foot, v_n is the normal of the foot at the point y, g is the acceleration due to gravity, and h_p is the depth of a point y below the surface of the water. These equations are evaluated numerically in the simulation. The interval of integration and the absolute vertical position of an infinitesimal area can be determined by the following:

$$a = \begin{cases} h & \text{if } |h| < 2r_f, \\ 2r_f & \text{if } |h| \geq 2r_f, \end{cases}$$
$$h_p = (h - (y - r_f))\cos\theta_f, \tag{4}$$

where θ_f is the angle of the foot measured counterclockwise from the vertical.

In the case of the compliant footpad, the area used in the integrand is different depending on the direction of the footpad's normal velocity. When pushing downward against the water, the footpad's normal vector and its velocity are in the same direction, and integration is performed as in (2) and (3). When the footpad pulls back, the area of integration is reduced due to the directional compliance of the footpad. In which case, $r_f = r_R$ in (2) and (3), where r_R is the reduced radius of the footpad, estimated to be 1/4 of the original radius.

Other forces, such as the surface tension and the shear force, are considered negligible. In particular, when the pull-off force is applied, the contribution to the drag force due to the surface tension γ has been examined and is at most about $2\pi r_f \gamma = 9.04 \times 10^{-3}$ N when the footpad becomes parallel to the water surface. This is less than 1% of the pull-off force caused by the hydrodynamic force. Also, since the Reynolds number is $Re = (2v_n r_f)/\nu = 7.2 \times 10^4$ where ν is kinematic

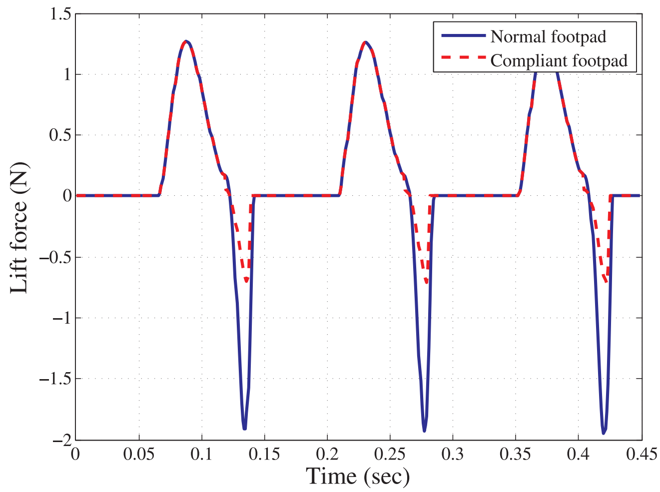

Fig. 4. The forces on a normal and compliant footpad in simulation with a running frequency of 7 Hz. The compliant footpad reduces the water contact area by folding when it pulls off, hence reducing the pull-off force.

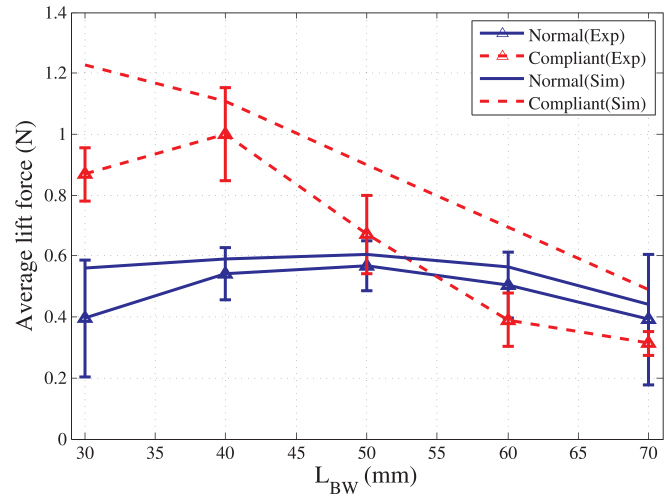

Fig. 5. The lift force is measured with the normal and compliant footpads while varying L_{BW} in experiment and simulation at 7 Hz. The compliant footpad generates higher average lift force due to reduction of the pull-off force.

viscosity of the water at room temperature with a 7 Hz running speed, it is reasonable to neglect the shear force due to the dominance of inertial effects in the fluid.

Figure 4 shows the simulated lift force during three leg rotation cycles when $L_{BW} = 50$ mm. By folding its feet, the pull-off force, or negative lift force, is reduced for the compliant footpad so that the overall lift force is increased. Furthermore, the average overall lift force is measured when varying L_{BW} at 7 Hz in Figure 5. The compliant footpad can generate up to 60% higher lift than the normal footpad at around $L_{BW} = 40$ mm. Figure 5 demonstrates how the simulated model predicts the experiment results. Average lift force is measured with fixed robot (no degree of freedom) at L_{BW} in experiment.

One of discrepancies between the two is that the compliant footpad does not show an optimal value of L_{BW} within the simulated model but it does in experiment. In reality, the sealing time required is about 0.103 seconds for $r_f = 20$ mm (Floyd and Sitti 2008; Glasheen and McMahon 1996b). When L_{BW} decreases, the time the foot is under the water increases, so the air cavity collapses before the foot is removed from water, which amplifies the pull-off force and decreases the net lift force. This tells us that if L_{BW} ever drops below a certain height, around 40 mm, the robot is unlikely to recover.

3. Roll Motion Analysis

In both simulations and the experiments in Floyd et al. (2006), the robot motion in the roll direction is observed to be highly unstable because its moment of inertia is small compared with the roll moments exerted by the water contact. The key purpose of this analysis is to determine a design for the robot which is stable in the roll direction and easily controllable. Since the previous model employs double-sided four-bar mechanisms with asymmetric leg configurations, a certain amount of roll angle variation is inevitable.

Obviously, if the model locomotes with a trot gait, in which diagonal pairs of feet touch the water simultaneously (Kimura et al. 1989), the roll moment is always negated due to the symmetry. In contrast, the worst-case scenario occurs when the robot uses a pace gait, where two legs on the same side touch the water simultaneously. All other gaits will fall between these two extremes in terms of exerted roll moment. In order to create a conservative design, only the pace gait will be examined during the roll motion analysis.

In this section, the generated roll moment is examined in experiment and simulation to determine the magnitude of the forces and torques. This information is then used to generate a conservative model of the roll motion, based upon the assumption of the pace gait. With this model, cautious bounds are placed on the sufficient moment of inertia to ensure stable roll motion. These conservative bounds are then used as a starting point to determine more easily attainable design specifications for a reasonable roll moment of inertia. In all experiments and simulations, the robot was free to rotate in the roll direction and it was constrained in all other directions to analyze the rolling stability only.

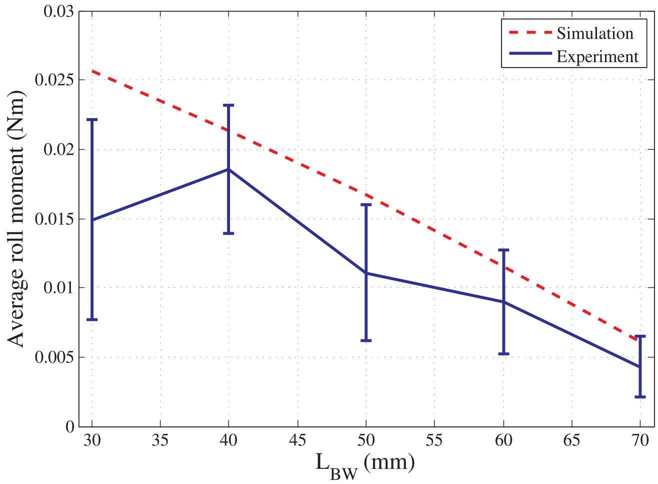

Fig. 6. Average roll moment at 7 Hz in simulation and experiment. Similar to the lift force measurement, a maximum roll moment is measured at $L_{BW} = 40$ mm.

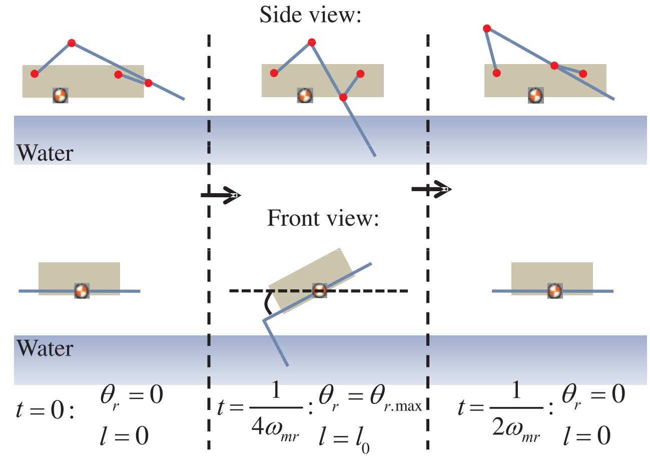

Fig. 7. Several schematic snapshots of the side and front views of the water runner when the modeled roll frequency is synchronized with the modeled running frequency. We assume that the maximum displacement from the tip of the footpad to the COM occurs at the maximum roll angle.

3.1. Experimental Roll Moment

The average roll moment is measured at varying values of L_{BW} in Figure 6. The moment of inertia with respect to the roll axis of the old model is 3.99×10^{-5} kg m^2 and the maximum average moment caused by the water interaction force is about 1.8×10^{-2} Nm when two legs on one side are synchronized. Hence, the maximum instantaneous angular acceleration along the roll axis can exceed 450 rad s^{-2} which is large enough to cause the robot to capsize. Similar to the lift force measurement for the compliant footpad, there is discrepancy between the experiment and the simulation, in which an optimal value of L_{BW} is observed in the experiment but is not present in the simulation. This is likely because of the same reasons in the lift force measurements, i.e. the foot is not pulling completely out of the cavity if the robot is too low into the water. For given robot design at 7 Hz, the lift force generated by the water interactions is at most around 1.4 N, so it is necessary to find the design which can endure the moment induced by that lift force operating at a distance equal to half the robot's width.

3.2. Roll Motion Modeling

The roll motion analysis is fairly complicated because it is a function of the running frequency, roll angle, instantaneous roll angular momentum, foot depth, footpad configuration, and average lift force. nonlinear relations with respect to each other, no closed form solution is currently known and it would be impractical to completely test the design space. achieve a complete analysis with full degree of freedom in simulation. Since all of these variables are coupled and have nonlinear relations with respect to each other, no closed form solution is currently available and it would be impractical to completely test the whole design space. Hence, a simple model that is generically similar to the roll motion but can be parameterized with respect to these variables is necessary. To do this, two assumptions are made.

Assumption 1. *The water interaction forces exist when the robot is tilted in a roll angle recovering direction.*

Assumption 2. *The instantaneous water interaction force is linearly proportional to the footpad depth in the water.*

Assumption 1 states that no matter what the leg configuration is, the water interaction force is always generated. Depending on the synchronization of the running frequency and the roll frequency, the water interaction forces occasionally do not exist, or the direction of the generated moment does not act to restore the robot. However, as long as the running frequency is similar to the body roll frequency, i.e. one stroke from each side can tilt the robot to the other side, Assumption 1 holds. This is shown schematically in Figure 7 with leg motion and body rotation synchronized. Note that this only happens when the roll moment of inertia is small compared with the roll moment generated by the water interaction force.

Figure 8 shows the hysteresis of the simulated lift force versus the height of the front left foot trajectory for one foot rotation cycle in simulation. Positive lift force is generated as the foot penetration depth is increased, and the pull-off force is generated during protraction. Two linearized forces

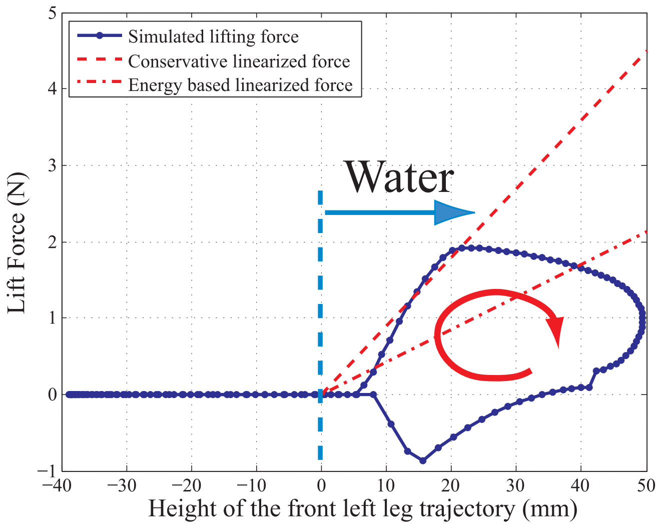

Fig. 8. The simulated lift force generated by the water interaction versus the penetration depth of the center of the foot during one footstep while running at 7 Hz. Also shown are two linearized forces based upon this simulation. While a conservative linearized force fits the maximum positive lift force, an energy based linearized force takes into account the total energy dissipated during water contact. These linearizations are used for spring constants in Equation (5).

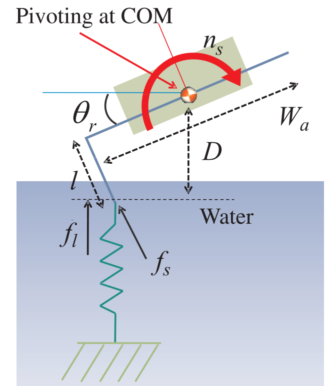

Fig. 9. Front view schematic of the robot during roll motion modeling. The water interaction force is modeled as a linear spring with the robot pivoting about a point 50 mm above the water's surface.

are shown and are used as spring constants. By using a conservative linearized force which overestimates the model's nonlinear lift force, we guarantee that Assumption 2 is an overestimation of the generated roll moment of the simulated robot. Since we want a model that can guarantee the stability of all configurations, we can prepare for the worst case by using this assumption. As a result of these assumptions, the water can be regarded as a linear spring.

Using the linearized spring-based water interaction model, a robot roll dynamic model is proposed. It is assumed that the robot pivots in the roll direction about an operating point, 50 mm above the water's surface at the COM of the robot as in Figure 9. This model can be parameterized as follows:

$$D = \frac{W_a \sin\theta_r}{2} + l\cos\theta_r,$$

$$K(f_{\max}) = 2 f_{\max}/(W_a \sin\theta_{r,\max} + 2 l_0 \cos\theta_{r,\max}),$$

$$f_l = K(f_{\max}) D, \quad f_s = f_l \cos\theta_r, \tag{5}$$

where

$$l = l_0 \sin\left(\frac{2\pi\theta_r}{4\theta_{r,\max}}\right),$$

where D is the linear displacement of the end of the leg, W_a is the width of the leg axis, θ_r is the roll angle of the body measured from the horizontal, l is the displacement from the tip of the footpad to the center of mass, $l_0 = 46.72$ mm is the maximum leg depth, $\theta_{r,\max} = 30°$ is the desired maximum roll angle, K is the effective spring constant of the water, f_l is the lift force, and f_s is the force applied to the linear spring.

As mentioned briefly before, a linearized force is used for the estimation of a spring constant. There are two ways to choose the maximum lift force, $f_{\max}$, at a given running frequency: a conservative method or an energy-based method. First, in the conservative method, $f_{\max}$ can be chosen as the sum of the maximum lift force and the minimum lift force. This is because the pull-off force on one side can potentially be coupled with the maximum lift force on the other side. Second, by using the total energy expended on the water, and hence on the robot, from Figure 8, in conjunction with the maximum displacement, an effective spring constant can be found, and the maximum force would be that constant multiplied by the maximum displacement. While the conservative method provides a higher spring constant because it overestimates lift force as much as possible, the energy-based method results in lower bound for the maximum lift force, i.e.

$$f_{\max} = \begin{cases} |f_{\text{lift, max}}| + |f_{\text{lift, min}}| & \text{for the conservative method,} \\ 2\int \frac{f_{\text{lift}} dx}{x_{\max}} & \text{for the energy based method.} \end{cases}$$

From f_s, the moment, n_s, is generated, and an ordinary differential equation can be obtained:

$$\begin{aligned} n_s &= -\frac{W_a f_s}{2}, \\ \ddot{\theta}_r &= \frac{n_s}{\mathcal{I}_{\text{roll}}}, \\ &= -\frac{K(f_{\max}) W_a^2 \sin 2\theta_r}{8\mathcal{I}_{\text{roll}}} - \frac{l_0 W_a}{2\mathcal{I}_{\text{roll}}} \sin\left(\frac{2\pi\theta_r}{4\theta_{r,\max}}\right)\cos^2\theta_r, \end{aligned} \tag{6}$$

where $\mathcal{I}_{\text{roll}}$ is the moment of inertia with respect to the roll axis. The angular momentum generated by the lift force causes a sinusoidal roll motion.

With the same constraints as the linearized model, a three-dimensional simulation which contains the full dynamics of the actual robot is performed to compare the resultant roll motion. Angular acceleration and angular displacement along the roll direction for a full cycle are inspected while varying the roll moment of inertia. It is certain that the linearized model has higher angular accelerations due to the lift force overestimation. Yet, differences are at most 15%, and angular displacement behaviors are almost the same. Therefore, the linearized roll modeling can be said to be valid enough to show actual the robot's roll motion (Park et al. 2008).

3.3. Roll Moment of Inertia Analysis

By varying the width of the robot, the roll moment of inertia and the mass are both affected. This effect is estimated by

$$W_a = W_0\left(1 + \frac{\Delta W}{W_0}\right), \tag{7}$$

$$m(W_a) = (m_0 - 2m_m)\frac{W_a}{W_0} + 2m_m, \tag{8}$$

$$\mathcal{I}_{\text{roll}}(W_a) = \mathcal{I}_0 \frac{m}{m_0}\left(\frac{W_a}{W_0}\right)^2, \tag{9}$$

where m is the increased mass, m_m is the motor mass, ΔW is an incremental increase in width with respect to the original width, and m_0, W_0, and $\mathcal{I}_0$ are the original mass, width, and roll moment of inertia, respectively. Using these, the modeled roll frequency, ω_{mr}, can be determined by solving (6) and is shown in Figure 10. Conversely, (6) can also be used to determine the required moment of inertia for stability at a given running frequency.

Equation (6) shows undamped oscillatory motion that is stable in the Lyapunov sense. Based on Assumption 1, the running frequency in the model, ω_{mru}, is the same as ω_{mr} for a given spring constant, K, which is a function of the maximum lift force. ω_{mru} can also be interpreted as the minimum running frequency to maintain the stability of the dynamics in (6). Moreover, the actual roll frequency, ω_r, is equal to or less than ω_{mr} because the model overestimates lift force, and hence the spring constant. Therefore, if

$$\omega_{ru} > \omega_{mru} = \omega_{mr} \geq \omega_r \tag{10}$$

where ω_{ru} is the actual robot running frequency, then the period of the roll motion is sufficiently long that the robot cannot flip completely over from a stroke on one side without the other side stroking first. As a thought problem, consider the case where the robot moves from a given maximum roll angle, $\theta_r = \theta_{r,\max}$ to the other side where $\theta_r = -\theta_{r,\max}$ during

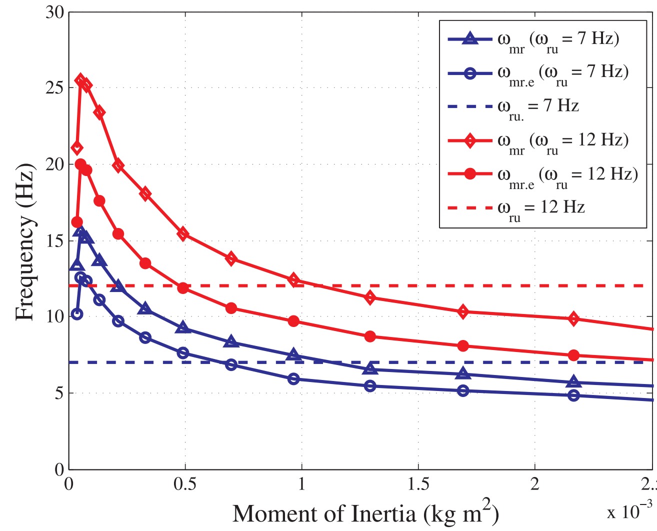

Fig. 10. Simulated relationship between the moment of inertia and the roll frequency at a running speed of 7 and 12 Hz using (6). Stability is guaranteed when $\omega_{mr} < \omega_{ru}$, and is likely when $\omega_{mr.e} < \omega_{ru}$, where $\omega_{mr.e}$ stands for the modeled roll frequency of the energy-based method.

$1/\omega_r$. During this period, at least one stroke in the recovering direction is necessary to provide an opposing angular moment. Otherwise, $\sup_{t\to\infty}\{|\theta_{r,\max}(t)|\} = \infty$. Therefore, in order to avoid this, the stroking period, $1/\omega_{ru}$, should be equal to or shorter than $1/\omega_r$. Thus, one must choose a moment of inertia such that (10), or $\omega_{mr} < \omega_{ru}$ holds true for stable roll motion (Figure 10).

To satisfy this requirement, the necessary roll moment of inertia would be 1.2×10^{-3} kg m^2 for the conservative method, or 7.0×10^{-4} kg m^2 for the energy-based method at $\omega_{ru} =$ 7 Hz, with slightly lower values for 12 Hz running. These inertia values are 30 and 18 times greater than the initial robots, respectively. From Equations (7), (8), and (9), the conservative inertia value would lead to a robot a total of 220 mm wide with a mass of 158 g. The energy method does little better, requiring a robot 18 cm wide with a mass of 134 g. Since both of these values used worst-case scenario estimates and linearizations, it is worth investigating what occurs when the non-linear foot–water interaction model is used instead.

Using 1.2×10^{-3} kg m^2 as a starting point, the roll moment was lowered in three-dimensional simulation, and the amplitude of the roll angle in steady state was recorded, as shown in Figure 11. During the simulations, since only drag force is considered in the water interaction, a high amplitude of roll angle can be recovered as long as it is less than 90°, which is observed when the roll moment of inertia less than 0.1×10^{-3} kg m^2. However, in reality, high damping force by water interaction reduces lift force, which makes the robot sink at such high roll angles.

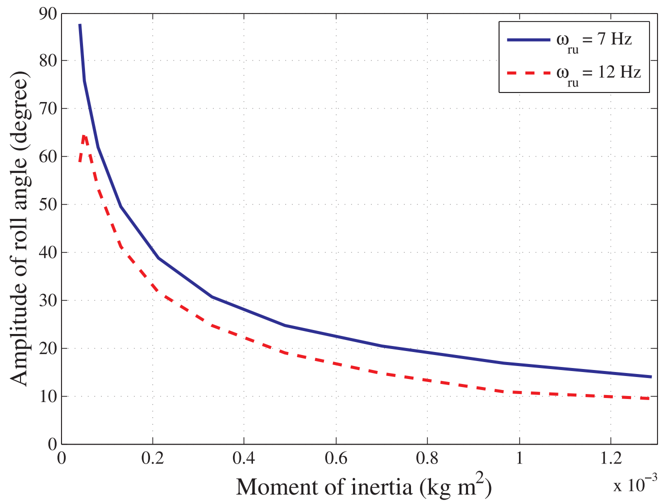

Fig. 11. Simulated maximum variation in roll angle while varying moment of inertia running at $\omega_{ru} = 7$ Hz and $\omega_{ru} = 12$ Hz. Steady-state oscillations fall within the presented maximum variations (which include transient behaviors).

With the desired condition of $|\theta_r|_{\max} = 30°$, this implies that only a roll inertia value of approximately 3.0×10^{-4} kg m^2 would be required. This implies using the methodology described above, a conservative estimate will produce a *sufficient* roll moment of inertia for the stability, but not a *necessary* moment of inertia. However, even this borderline design would require a robot 130 mm wide with a mass of over 105 g. It is clear from these results that the body style used in previous designs was inappropriate with regards to stabilizing roll motion. Hence, a new body design, with motors (the heaviest single components) placed towards the sides instead of centrally located was fabricated, and is described in detail in Section 5.

4. Pitch Motion Analysis

A second problem of the water runner is instability of the pitch motion which causes the robot to flip backward. This is due to a net pitch moment around the COM generated by the lift and thrust forces of each of the four feet.

Similar to the biological system, we claim that a tail could play a crucial role in stabilizing pitch motion. We propose the introduction of a tail which is plunged into the water behind the robot which generates a backward drag and a restoring pitch moment. The objective of the tail is to generate enough clockwise pitch moment to negate the counterclockwise pitch moment generated by the four feet, with the reference frame used in Figure 12. Also, it should be able to make the average body pitch angle of the robot zero. We examine both a stationary tail placed in an optimal location to stabilize motion, and a tail which can actively change its position to compensate for disturbances.

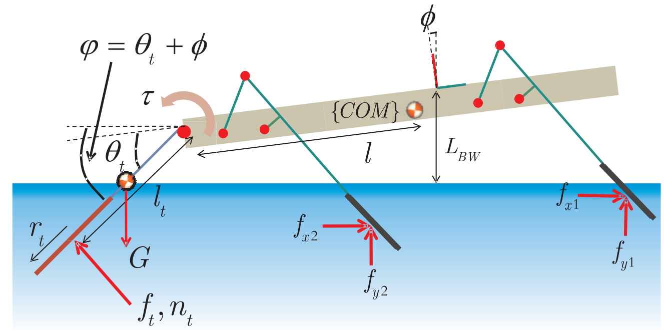

Fig. 12. Side view schematic of a water runner with a tail to control the pitch moment using drag force. Specified dimensions are in Table 1.

In this section, the generated pitch moment is examined in both experiment and simulation to determine the magnitude of the forces and torques. A conservative model of the tail forces are then developed and compared with experiment. Criteria are established and used to select appropriate parameters for the design of the tail. Both passive and active tails are then examined for effectiveness within simulation and compared. In addition, roll motion is assumed to be stable by employing high enough roll moment of inertia for the pitch analysis. This assumption enables to analyze roll and pitch motion separately. It can be shown in Figure 22.

In all experiments and simulations, the robot is free to rotate in the pitch direction, but all other degrees of freedom are constrained to analyze the pitch stability only.

4.1. Pitch Moment

As shown in Figure 12, the forces exerted on feet can be decomposed into horizontal forces, f_{x1} and f_{x2}, and vertical forces, f_{y1} and f_{y2}. Here f_{x1}, f_{y1}, and f_{x2} all generate a pitch moment in the counterclockwise direction and only f_{y2} does so in a clockwise direction at the COM. Many quadrupedal or bipedal robots use redundant joints to place the COM or the zero moment point (ZMP) at a desired position which can achieve balance (Kajita et al. 2003; Park and Youm 2007). However, the water runner robot cannot have several redundant actuators and links due severe restrictions on the weight. All joints are used for generating the lift and the propulsion forces. To stabilize the pitch motion, an additional component which can negate the moment around the COM is necessary. We propose a tail generating a drag force which can produce a clockwise direction moment (Figure 12).

Figure 13 shows the required average pitch moment measured in both simulation and experiment which needs to be

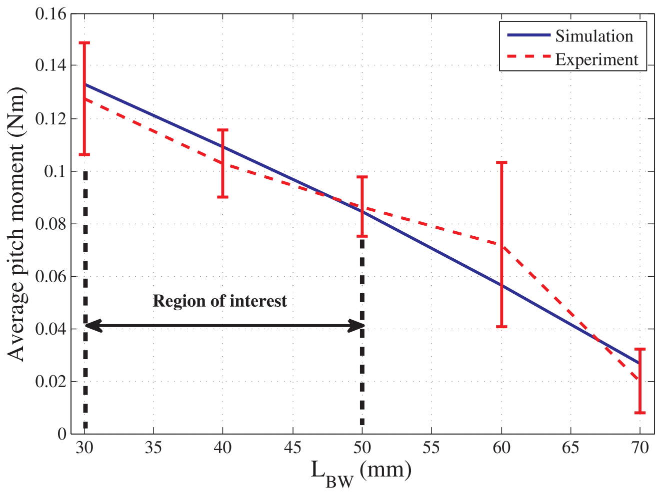

Fig. 13. The average pitch moment is measured while varying L_{BW} in both simulation and experiment. Data indicate how much pitch moment should be generated by the tail at a running frequency of 7 Hz.

balanced. Hence, the tail should be able to generate an average moment of about 0.13 Nm. For the experimental setup, average pitch moment is measured at varying values of L_{BW}.

4.2. Tail Dynamics

The tail is assumed to be made of a lightweight material, and does not shift the location of the combined COM. Unlike the footpad, we assume that the hydrostatic drag force is not a concern because the motion of the tail should be sufficiently slow so that no air cavity is created. The hydrodynamic drag exerted on the tailpad is proportional to square of the instantaneous normal velocity of the tailpad plane and the contact area with the water:

$$f_t = C_D \rho \int_0^{a_t} \sqrt{r_t^2 - (y - r_t)^2} v_n |v_{t.n}| \, dy, \tag{11}$$

$$n_t = C_D \rho \int_0^{a_t} (y - r_t) \sqrt{r_t^2 - (y - r_t)^2} v_{t.n} |v_{t.n}| \, dy, \tag{12}$$

where

$$v_{t.n} = v_h \sin\varphi + (l_t + r_t - y)\dot{\varphi},$$

$$\varphi = \theta_t + \phi,$$

where $C_D = 1.1$ is the drag coefficient of a disk in free stream (Munson et al. 2002), f_t and n_t are the force and the moment, respectively, generated by the tail and taken at the center of the tailpad, r_t is the radius of the tailpad shown in Figure 12, l_t is the length from the tail's attachment point at the body to the center of the tailpad, θ_t is the tail's angle relative to the robot body, ϕ is the pitch angle of the robot body, and v_h is the horizontal robot body velocity as shown in Figure 12. The interval of integration can be determined by the following:

$$a_t = \begin{cases} h_t & \text{if } |h_t| < 2r_t, \\ 2r_t & \text{if } |h_t| \geq 2r_t, \end{cases}$$

where h_t is the distance from the lowest point of the tail to the water surface within the tail's reference frame. The dynamics of the tail angle and the pitch angle can be described:

$$\ddot{\theta}_t = \frac{1}{\mathcal{I}_t}(\tau + l_t f_t(\varphi, \dot{\varphi}) + l_c G \sin\varphi + n_t), \tag{13}$$

$$\ddot{\phi} = \frac{1}{\mathcal{I}_p}(n_{\text{tail}} - n_{\text{COM}}), \tag{14}$$

where $f_t(\varphi, \dot{\varphi})$ and G are the forces acting on the tailpad from (11) and gravity, respectively. Here $\mathcal{I}_t$ is the moment of inertia of the tail and l_c is the length from the tail's attachment point to the body to the tail's COM (Figure 12). Here n_{tail} is the moment generated by the tail measured at the COM, n_{COM} is the moment around the COM caused by the water interaction force with the feet, and $\mathcal{I}_p$ is the pitch moment of inertia of the robot.

4.3. Approximate Tail Pitch Moment

The approximate pitch moment, n_g, generated by the tail and measured at the COM with respect to the angle between the tail and the water surface, φ, can be estimated by

$$n_g = \begin{cases} 0 & \text{if } \varphi \leq \varphi_{\min}, \\ n_{gt} & \text{if } \varphi > \varphi_{\min}, \end{cases} \tag{15}$$

where

$$n_{gt} \approx \frac{1}{2} C_D \rho \pi r_t^2 (l \cos\theta_t + l_t)(v_h \sin\varphi)^2 A,$$

$$A = \begin{cases} \frac{r_t + l_t - y/\sin\varphi}{2r_t} & \text{if } (r_t + l_t - y/\sin\varphi) < 2r_t, \\ 1 & \text{if } (r_t + l_t - y/\sin\varphi) \geq 2r_t, \end{cases}$$

$$\varphi_{\min} = \sin^{-1}\left(\frac{y}{l_t + r_t}\right),$$

$$y = \text{Level} - l \sin\phi,$$

here A is the ratio of the submerged area and $\varphi_{\min}$ is the minimum tail angle required to generate the water interaction force based on the robot geometry and the position relative to the water.

The horizontal velocity of the robot is assumed to be 1 m s^{-1}, which has been achieved in experimental trials.

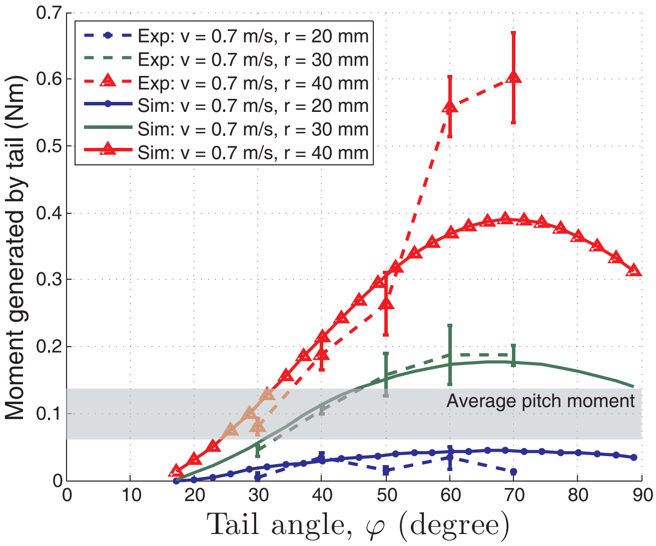

Fig. 14. Experiment and simulation results of pitch moment generation versus tail angle for three tail radii at a running frequency of 7 Hz. The moment generated by the tail can be approximated (15) as a function of r_t, v_h, and φ. The minimum tail radius which can generate enough pitch moment is slightly less than 30 mm. Running speed is 1 m s^{-1}.

4.4. Passive Tail Design

For simplicity, we first propose a passive, circular tail which is attached at the end of the robot body at specific fixed angle.

Figure 14 shows the pitch moment generated by a tail at varying tail angles and radii when the robot body is aligned to the horizontal, i.e. $\phi = 0°$. The shaded area represents the average pitch moment generated by the water interaction of the feet within the region of interest, 0.08–0.14 Nm, in Figure 13. Since a 20 mm radius tail cannot span the range of average pitch moments, it is too small to be used for the tail.

For the experiment, the tail with some angle at constant speed of water flow is set up to measure pitch moment generated by drag force of tail when all directions of motions are constrained. There is a discrepancy between simulation and experiment for the 40 mm tailpad. The observed pitch moments are much higher than in simulation. The likely reason is that an air cavity behind the tailpad is created due to its size. As the Reynolds number of the tailpad increases, the fluid flow separates from the back side of the tailpad, and an air cavity is created. This results in a hydrostatic pressure drop across the tailpad, which leads to a higher generated pitch moment.

To determine an upper bound for the radius of the tailpad, Figure 15 is used. If the horizontal force generated by the tail, f_{t_x}, is greater than the average propulsion force generated by legs, $\overline{f_p} = 0.68$ N, it will decelerate the robot. In order for $f_{t_x} < \overline{f_p}$, the tail angle, φ, should be limited. Here f_{t_x} can be approximated by:

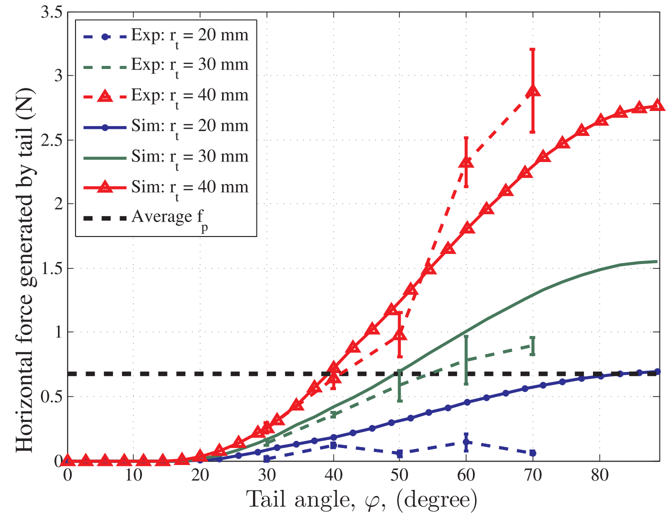

Fig. 15. Experimental and simulated horizontal tail forces versus tail angle for three tail radii. To satisfy the $f_{t_x} < \overline{f_p}$ criterion, the tail angle should be limited. Running speed is 1 m s^{-1}.

$$f_{t_x} \approx \frac{1}{2} C_D \rho \pi r_t^2 v_h^2 (\sin\varphi)^3 A. \qquad (16)$$

If the radius of the tailpad is greater than 40 mm, the range of tail within the limits defined by $f_{x_t} < \overline{f_p}$ cannot span the range of average pitch moments. Furthermore, the larger the radius, the heavier the tail. Thus, we select the smallest radius of tailpad, 30 mm, which we know can span entire range of average pitch moments while not generating excess negative horizontal force.

Since there are two variables, θ_t and ϕ, associated with (15), there are an infinite number of equilibrium points which balance the average pitch moment, i.e. $n_{\text{tail}} = n_{\text{COM}}$, as shown in Figure 16. This also implies that if $-15° < \phi < 25°$, then an equilibrium point exists. However, the desirable robot posture is only where $\phi = 0°$ because this causes the robot to be aligned in the horizontal direction. In order to be more accurate, we observed the pitch offset angle, ϕ_{off}, in simulation at various tailpad radii while varying the tail angle, as shown in Figure 17. A tailpad with a radius of 30 mm at an angle of 31° maintains the robot posture near horizontal.

Figure 18 shows the simulated result of the pitch motion with a passive tail. When $r_t = 30$ mm and $\theta_t = 31°$, the average pitch offset angle, ϕ_{off}, becomes almost zero and the pitch motion with the passive tail is stable.

4.5. Active Tail Design

The passive tail can generate the required average pitch moment to stabilize the pitch motion of the robot in steady state.

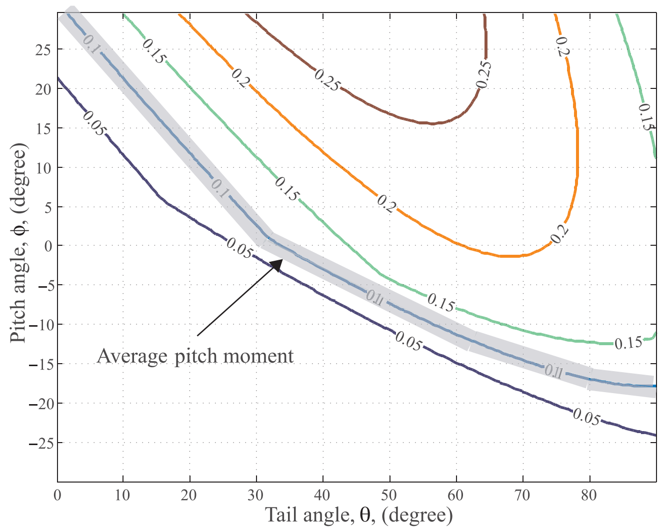

Fig. 16. Simulated isolines representing the same pitch moment generated by the tail and derived by (15) when $r_t = 30$ mm and a 7 Hz running frequency. There are infinite equilibrium points where the pitch moment is negated because it depends on two variables, θ_t and ϕ (the average pitch moment generated by feet is 0.08–0.14 Nm). To correct the robot posture, we are specifically interested where $\phi \approx 0°$.

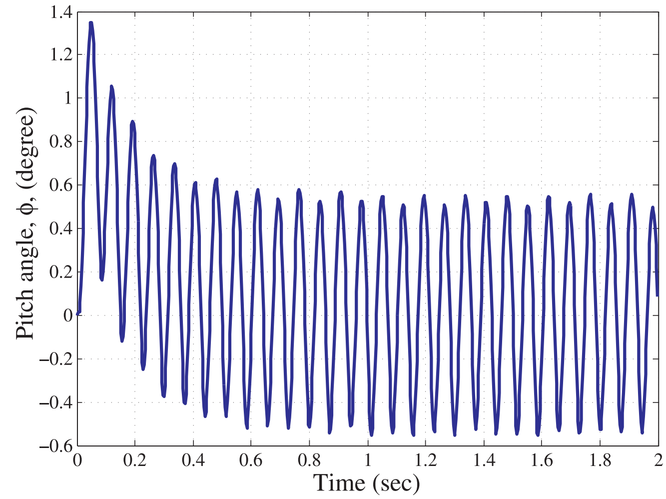

Fig. 18. When $r_t = 30$ mm, $\theta_t = 31°$, at a 7 Hz running frequency, the simulated average pitch offset angle, ϕ_{off}, becomes almost zero and the pitch motion with the passive tail is stable.

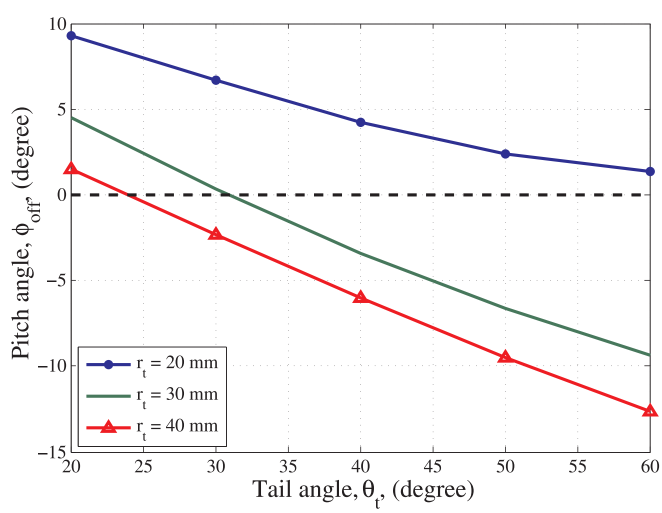

Fig. 17. The simulated average body pitch offset angle, ϕ_{off}, can be a criterion for choosing the tail angle, θ_t. When $\phi_{\mathrm{off}} = 0°$, the tail angle necessary to cancel the net pitch moment around the COM can simultaneously keep the robot body horizontal.

However, if there is a disturbance, i.e. varying horizontal velocity and/or changing the average pitch moment by adjusting the gait of the robot, there is no way to control the robot pitch or recover its initial body orientation once lost. In order to cope with these, an active tail to control the pitch motion using sensory feedback is proposed. This tail should cancel the net pitch moment around the COM and also correct the robot posture. By measuring the angular acceleration around the COM, and knowing the pitch moment of inertia, the pitch moment around the COM can be deduced, and the desired pitch moment the tail must generate to correct the robot posture can be computed. Then, the desired tail angle can be determined by solving the non-linear equation (15) using a Newton–Raphson non-linear equation solver. We propose the moment average tracking proportional derivative (PD) controller by applying torque at the tail joint:

$$\tau = -k_p(\varphi_d - \theta_t) - k_d(-\dot{\theta}_t) - l_c G \sin\varphi, \qquad (17)$$

where

$$\varphi_d = \texttt{NRsolve}(n_d),$$

$$n_d = n_{gt} + \frac{1}{T}\int_{t-T}^{t} -n_{\mathrm{COM}}\, dt.$$

Here $\texttt{NRsolve}(n_d)$ is the Newton–Raphson non-linear equation solver which returns a solution corresponding to the equation n_d, the desired moment from the tail. The reason why θ_t appears instead of φ in (17) is that this can rectify the posture, i.e. $\varphi_d = \theta_d$, if $\phi \to 0°$ as $t \to \infty$. Here T is the period of time over which to take an average.

The desired moment is the sum of the estimated moment generated by the current tail angle and the average pitch moment at the COM. The average moment at the COM represents the overall net pitch moment which causes the robot to become gradually tilted backwards. Integrating the moment measured at the COM over time, the pitch motion of the robot becomes more stable and robust since it does not track noise and high-frequency vibrations caused by the motion of the legs. A small change of the tail angle, θ_t, can control the robot pitch moment. (After all, the controller becomes similar to the passive tail if $T \to \infty$.) Since the variations of θ_t are small, the pitch motion also becomes more stable. However, simply increasing T causes slow responses to disturbances. Therefore, one should carefully select a value of T that is appropriate for the system. We found a reasonable value of T of about 0.3 s when running at 7 Hz, which shows stable pitch motion and desirable performance (Park et al. 2009). Since $T = 0.3$ s, the desired moment during the initial 0.3 s startup varies greatly, as in the peak shown at ~0.15 s in Figure 20. However, after 1 s, pitch motion reaches steady state in simulation.

By choosing appropriate PD gains, $k_p = 1$ and $k_d = 0.007$, the tail angle, θ_t, can be controlled to track a desired angle, φ_d so as to negate the instantaneous pitch moment at the COM. This controller results in a pitch angle, ϕ, which is stable with a maximum $\pm 10^\circ$ variation as the generated moment, n_g, tracks the desired moment, n_d.

As discussed in the passive tail case, the number of moment equilibrium points is infinite. While the tail controller can move an arbitrary state to an equilibrium point, that point is not necessarily a desirable point where $\phi_{\text{off}} = 0^\circ$. Thus, an additional controller that negates any ϕ offset is necessary. Also, if the robot's horizontal velocity is not constant, the solution of the non-linear equation (15) can be inaccurate. To account for these, a velocity estimator which updates the current horizontal velocity estimate by measuring ϕ is proposed. If the actual velocity, v_h, is reduced, the average ϕ becomes greater due to the fact that the current tail angle, θ_t, is insufficient to generate the necessary stabilizing pitch moment. This tends to make the robot become inclined with $\phi_{\text{off}} > 0^\circ$. In order to correct its posture, the robot needs to estimate how much v_h is reduced and apply more torque to the tail so as to maintain a steeper θ_t, and vice versa for increased v_h. The velocity estimator is updated as follows:

$$v_h = v_h + k_{v_p}\phi + k_{v_d}\dot{\phi}, \tag{18}$$

where k_{v_p} and k_{v_d} are the PD gains. This estimator can cope with varying v_h and also negating ϕ_{off}. Figure 19 shows the velocity estimator tracking the actual v_h in simulation. There is an offset in the estimated velocity, $v_{\text{off}} \approx 0.1$ m s^{-1} due to the error between the approximated pitch moment n_g and the actual pitch moment n_t, but the controller still corrects ϕ_{off}.

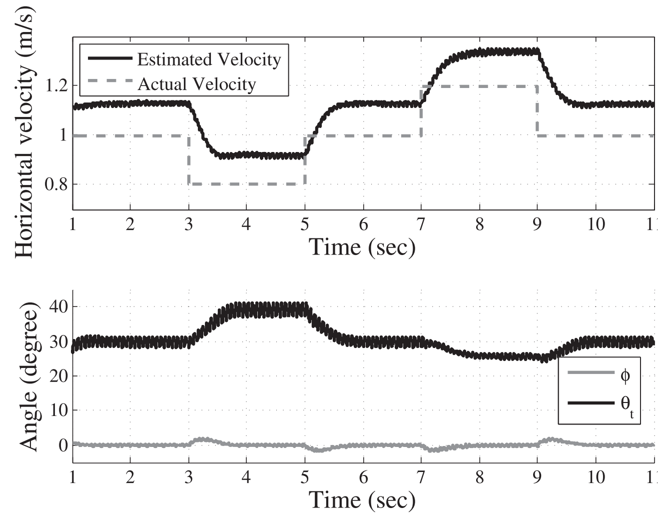

Fig. 19. The actual and estimated velocities versus time for the active tail controller in simulation. The corresponding simulated pitch angle, ϕ, and tail angle, θ_t, are also shown. The actual velocity v_h is changed every 2 seconds in simulation.

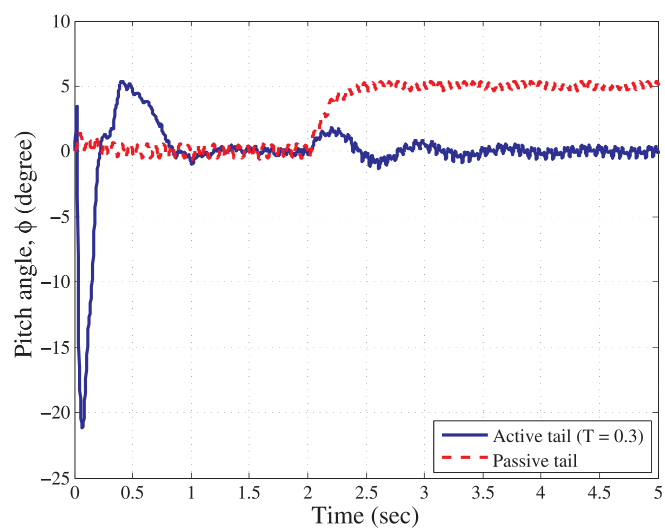

Fig. 20. The simulated change in body pitch angle when using either a passive or active tail during a step change in velocity. The velocity is decreased at time $t = 2.0$ s from 1 to 0.8 m s^{-1}.

4.6. Comparison of Passive and Active Tail Designs

The active tail requires a gyroscope and an accelerometer (2–3 g) at the COM and an actuator (~4 g) at the end of the robot body, which increases the mass by at least ~8 g or about 15% of the total mass. Furthermore, the root finding process of the Newton–Raphson non-linear equation solver uses iterations until a zero is found, which takes time depending on how abruptly the desired moment, n_d, changes. Also, all sensory feedback and algorithms would have to be implemented on a micro controller that has limited speed and memory and adds additional weight. One advantage of the active tail is its capability to cope with disturbances, but the advantage this provides does not seem to be significant. The magnitude of the pitch offset angle is at most 5°, as shown in Figures 20 and 26 when subjected to a velocity change of $\sim$ 0.2 m s^{-1}. Even though the active tail plays a role, the payload and computational expenses are too high when compared with the gains provided by the passive tail. Thus, the necessity of the active tail is debatable. However, if the system becomes more sophisticated, the active tail can be used to contribute high-level pitch motion control. Also, as far as amphibious locomotion is concerned, the active tail is an important tool to locate the COM and to balance on land. Since the current objective is to verify and demonstrate how the tail stabilize pitch motion on the surface of water, a passive tail is employed in experiments where the additional controller, sensor and actuator that would increase the weight and complexity of the robot are avoided in this paper.

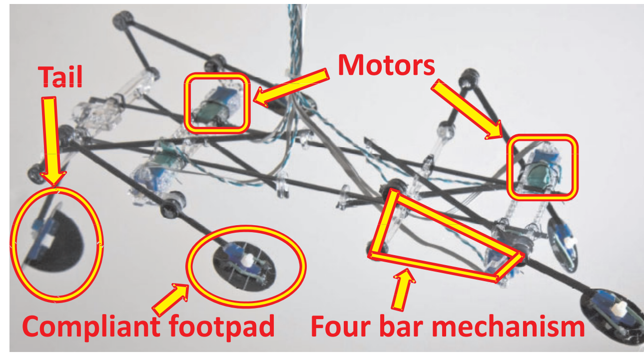

Fig. 21. Photograph of the new design of the water runner robot with the increased roll moment of inertia and the addition of a tail.

5. New Robot Body Design

Using the developed roll and pitch dynamics analysis, a stable quadruped robot is proposed. As a result of the roll motion analysis, it was found that the roll moment of inertia greater than 1.2×10^{-3} kg m^2 using a conservative method led to stable roll motion for the robot's parameters. However, this value is practically impossible to achieve due to the constraints on the mass of the robot, which should be less than 100 g for the legs to lift it. Since we overestimated the water interaction force and assumed the worst-case scenario for the gait, this estimate represents a sufficient but not necessary condition for the roll stability. Hence, the required moment of inertia can be reduced somewhat, as seen in the plot of the roll motion, Figure 10. If we apply an energy-based roll stability criteria, a roll moment of inertia of 7.0×10^{-4} kg m^2 is calculated for stability, which is feasible. The exact requirements for stability are difficult to determine because the equations used do not take into account instantaneous roll moment or any damping effects caused by drag in air or water.

In order to maximize the roll moment of inertia for the robot, we added two motors and placed all four far from the COM of the robot, as shown in Figure 21. As a result of the new design, the roll moment is increased to 5.05×10^{-4} kg m^2 with a total mass of 100 g. Since the right and left legs are not exactly synchronized with a 180° phase shift, a continued pace gait is not guaranteed. Power is provided by external batteries (not shown).

To correct the pitch instability, a tail pad 30 mm in radius was added to the robot, as shown in Figure 21. This tail pad was placed at an angle of approximately 30° relative to the robot at the end of a 10 cm long piece of carbon fiber. In addition to the cross-sectional pad, a semi-circular rudder with a radius of 30 mm was included as part of the tail. This was added in a further effort to damp rotation motion, and may potentially be used as a steering device in the future.

5.1. Experimental High-speed Video Footage Analysis

The motion of the robot at steady state was recorded with a high-speed video camera to test for roll and pitch stability. External power was supplied and each leg rotates at 7 Hz. Figure 23 shows roll motion of the robot for 194 ms, or slightly over one leg rotation cycle. The robot gait was set to a pace gait and compliant footpads were used. Even though there are roll angle variations, the maximum magnitude does not surpass 20°. For the pitch motion, a passive tail is used and is shown in Figure 22, which shows the water runner robot running at 7 Hz towards the right for 342 ms, or slightly over two complete leg cycles. Pitch motion is stabilized by the tail interacting with the water. The pitch and roll motions are observed to be stable.

6. Robustness Analysis

To examine the new robot's robustness, the new robot model is tested in simulation for its response to two types of disturbance: waves and running frequency variations. When running on an uneven water surface, it is more challenging to achieve stability because the lift force is no longer symmetric. Moreover, running frequency variations, which may occur due to imperfect velocity control of the DC motors or variations in the motor parameters, can cause changes in gait and asymmetric lift forces.

For roll motion simulation, constraints of the robot are applied slightly different from previous roll simulation. It is able to not only rotate in the roll direction but also move along a vertical axis, which shows roll and lift behaviors. For the pitch motion, the robot can rotate freely in the pitch direction about the COM and is constrained in all other directions.

6.1. Simulated Wave-like Disturbance

Let us define waves depending on the direction of propagation. Frontal waves oscillate along the length of the robot and lateral

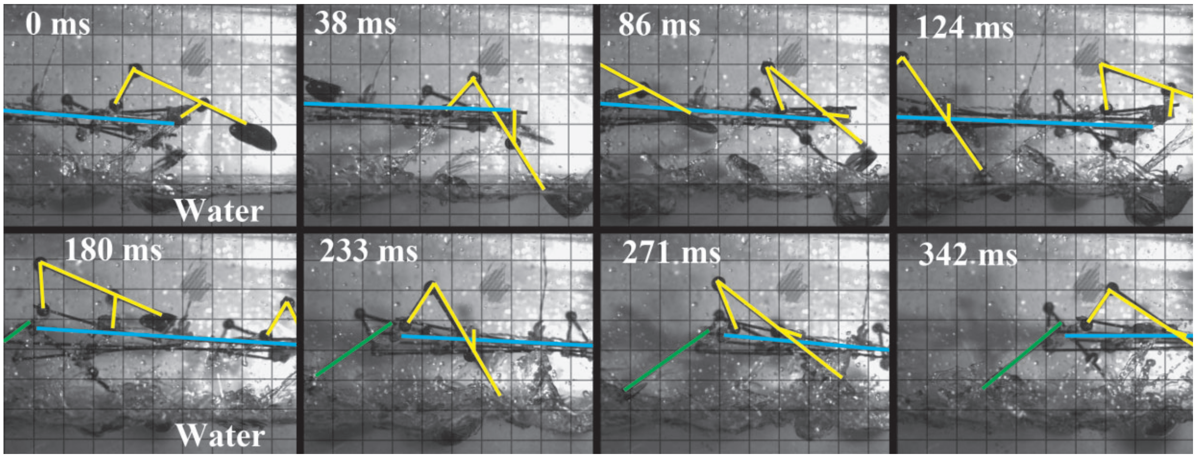

Fig. 22. Side-view high-speed video footage of the new robot's pitch motion. The four-bar legs, the tail and the robot body are highlighted. The body pitch angle, ϕ, is around zero when $r_t = 30$ mm and $\theta_t = 30°$ so the posture of the robot is maintained due to the pitch moment generated by the passive tail.

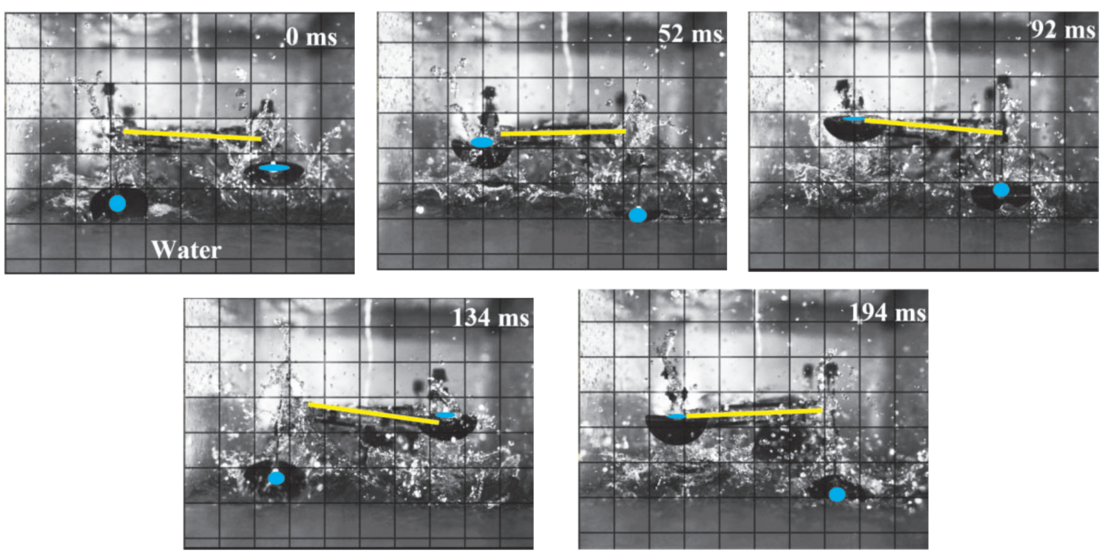

Fig. 23. Front-view high-speed video footage of the new robot's roll motion. The roll angle, θ_r, is at most about 20° with the increased roll moment of inertia, 5.05×10^{-4} kg m^2 for the new design. The robot body orientation and position of the feet are highlighted.

waves oscillate along the width of the robot. Wavelengths are set so that the positions where the feet touch the water are 180° out of phase, which maximizes the lift force differences which can occur, and are shown in Figure 24. The wave equation can be described as

$$W(t, x, z) = A_w \sin\left(\frac{2\pi}{T_w}t - \frac{2\pi}{\lambda_l}x - \frac{2\pi}{\lambda_f}z\right), \qquad (19)$$

where A_w is the amplitude of the wave, T_w is the period of wave, which is chosen to be 0.5 s, and $\lambda_l = 245$ mm and $\lambda_f = 444$ mm are the lateral and the frontal wavelengths, respectively. The amplitude A_w is examined from 0 to 30 mm because if the amplitude of a wave is greater than 30 mm, the full trajectory of each foot, shown in Figure 3, will be almost submerged when operating at $L_{BW} = 50$ mm. In such a case, the real system's lift force would not fit with simulations because the feet would not escape the air cavity collapse.

The roll motion is more sensitive to disturbances from lateral waves than from frontal waves because lateral waves result in asymmetric roll moments. The maximum recoverable roll

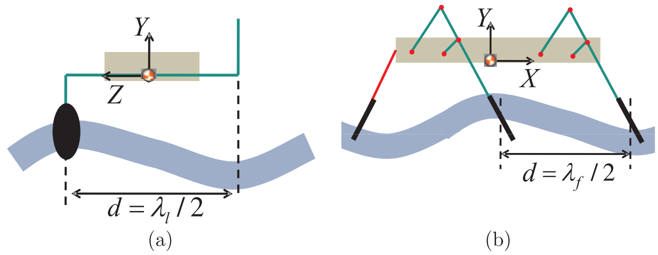

Fig. 24. Simulated waves are defined based upon two forms, (a) the lateral and (b) the frontal waves, which depend on the direction. Wave lengths are based upon the maximum displacement which can occur between two feet.

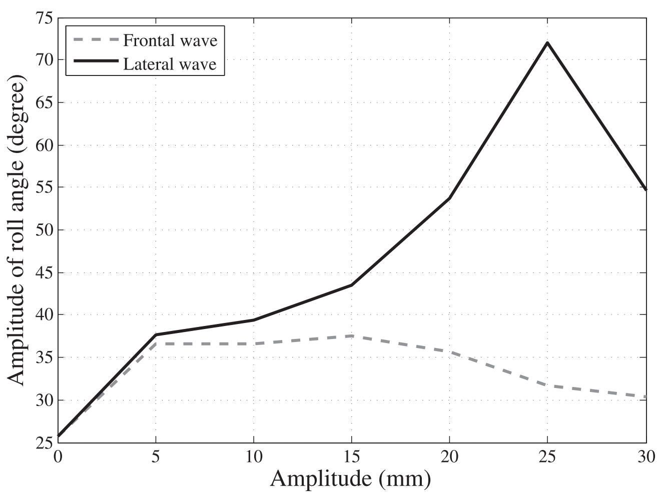

Fig. 25. Simulated roll angle variation for lateral and frontal waves of varying amplitude (running frequency = 7 Hz). Values have been horizontally offset slightly to facilitate viewing.

angle in reality is approximately $\pm 45^{\circ}$, an angle which would cause the footpad trajectory to be fully submerged, and the air cavity creation condition would not be held. As shown in Figure 25, a lateral wave amplitude slightly higher than 15 mm would be required to cause the amplitude of the roll angle to exceed 45°.

Conversely, pitch motion is more sensitive to frontal waves which yield different water interaction forces between the front and rear footpads. However, these waves do not directly affect the pitch motion because components of the water interaction forces related to the pitch moment on each footpad are coupled, as discussed before. In addition, since the pitch moment of inertia is about 10 times higher than the roll moment of inertia, the pitch angle variation is not significant relative to the roll angle variation. In this case, the active tail plays an important role in maintaining the pitch offset angle near zero while the passive tail average angle varies, shown in Figure 26. As

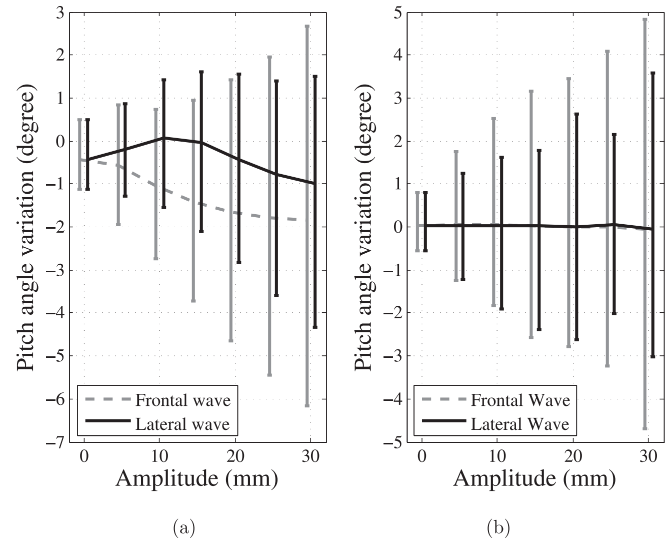

Fig. 26. Simulated pitch angle variation for lateral and frontal waves of varying amplitude for both the (a) passive and (b) active tail designs (running frequency = 7 Hz). Values have been horizontally offset slightly to facilitate viewing.

far as the pitch motion is concerned, the wave cannot disturb the system enough to create instabilities.

6.2. Simulated Running Frequency Variations

The DC motors, equipped with potentiometers, are controlled to maintain the same velocity using the optimal PD control. Nevertheless, uncertainties such as sensor noise, payload, and motor response can result in difference in the motors' velocities. This causes running frequency variations. In order to investigate the worst-case scenario, the robot is assumed to be running with a pace gait and the legs on only one side will have a different frequency. As shown in the wave modeling, since the roll motion is more disturbance-sensitive than the pitch motion, only the effects of running frequency variations on roll motion will be examined.

Equation (1) shows that the drag force acting on the footpad is proportional to square of the normal velocity, which is in turn proportional to the running frequency. The roll moment is proportional to the lift force which is also proportional to the drag force. Thus,

$$M_r \propto f_l \propto v_n^2 \propto \omega_{ru}^2, \tag{20}$$

where M_r is the roll moment and ω_{ru} is the running frequency. If ω_{ru} is the same on both sides, the average roll moment, $\bar{M}_r$, is negated. However, if there are variations in running frequency, $\Delta\omega_{ru}$, this creates an overall roll moment which can cause roll motion instabilities. The overall roll moment is

$$\bar{M}_r \propto 2(\Delta\omega_{ru})\omega_{ru} + (\Delta\omega_{ru})^2. \tag{21}$$

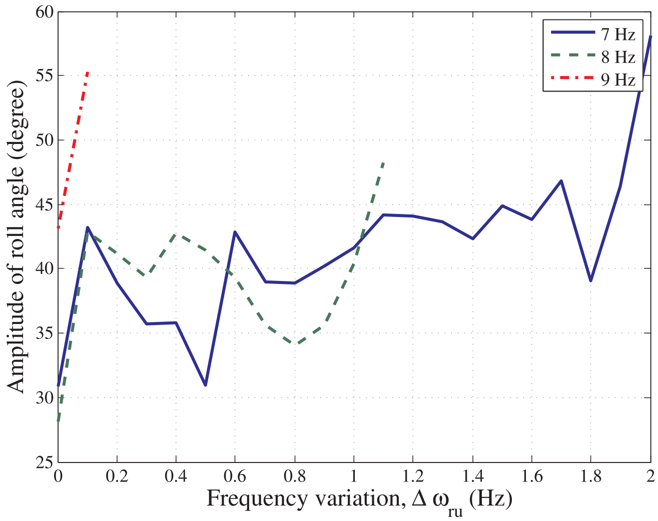

Fig. 27. Simulated amplitude of roll angle while varying the frequency of the legs on one side of the water runner. The responses for three different nominal velocities are displayed.

Equation (21) states the roll motion is more sensitive at a higher running frequency for a given frequency variation, and vice versa.

Figure 27 shows the amplitude of the roll angle ($\sup_{t\to\infty}\{\theta_r(t)\}$) with increasing ω_{ru}. While the roll motion is stable with up to 1.6 Hz variations at 7 Hz ($|\theta_r| \leq 45°$), it diverges at lower frequency variations when the running frequency is increased (1.2 and 0.2 Hz at $\omega_{ru} = 8$ and 9 Hz, respectively).

7. Discussion

Since both instabilities of roll and pitch motions are essentially caused by the force exerted at feet simultaneously, two motions may be coupled and separate analyses may not be enough to address total stability. The analysis performed here assumes only one degree of freedom in each situation so that appropriate experimental setups could be constructed to test the accuracy of the models estimates on moment generation. While a real system would have larger numbers of degrees of freedom, building experimental setups which would allow free motion while simultaneously measuring forces would be difficult if not impractical. In addition, this work is concerned with addressing the instabilities in a methodical manner, one at a time. Any simulation or experiments which allowed full freedom at the outset would not allow isolating the causes and effects of the two separate instabilities efficiently.

Therefore, each simulation and corresponding experiments are performed in constrained systems. For roll motion, a robot model was suspended at a set height above the water in a system which allowed roll rotation around the COM. The roll moment was then measured as the height was varied, to produce the experimental data shown in Figure 6. For pitch motion, similar experiments were performed with a model only allowed to rotate in the pitch direction, to produce the experimental results shown in Figure 13. To improve stability, design parameters are selected so as not to affect the other's stability, i.e. the roll moment of inertia is symmetric in the pitch direction and the tail is symmetric in the roll direction.

To demonstrate the stability of the final design, running with full degree of freedom is tested and independency of pitch and roll motions is observed in high-speed video footage shown in Figures 22 and 23. By increasing the roll moment of inertia, roll variation becomes small enough not to influence pitch motion at all and tail implementation results in small pitch variation which affects negligible roll motion.

8. Conclusions and Future Work

A water runner robot inspired by basilisk lizards was devised to demonstrate a water running capability based upon generating drag forces, not buoyancy. In this paper, the stability of roll and the pitch motion were analyzed. To understand the dynamics and to control motions, mathematical models were developed and various numerical techniques were used. Also, several experimental models were tested to validate the simulation results. The water interaction force was computed based on the drag equation. Owing to its small roll moment of inertia, the previous robot model was unstable. By making two modeling assumptions, we modeled the water as a linear spring and provided criteria to choose the moment of inertia for roll stability. Furthermore, the geometry of the water interaction forces and the location of the COM caused unstable pitch motion. Two types of tail, one passive and one active, were employed to compensate for the pitch moment at the COM. The passive tail was fixed at the end of the robot body at a specified tail angle with a given radius, whereas the active tail could change its angle. The average pitch moment provided a method to choose the radius of the tail and the average pitch offset angle showed which tail angle was appropriate. Since the passive tail could not compensate for disturbances, the active tail could more effectively stabilize pitch motion and maintain body orientation. According to the design parameters provided by the roll and the pitch analyses, a new design of the water runner robot was introduced and examined for robustness for disturbances due to waves and running frequency variations.

As future work, the function of the rudder in the robot tail for steering with an actuator attached to the tail and improved roll stability and yaw motion control will be studied. An amphibious quadruped water runner robot and a bio-inspired autonomous control method for its amphibious locomotion in unstructured environments will be developed. These quadruped mobile robots will be used in search and rescue and exploration applications in the future.

Acknowledgments

The authors would like to thank Lee Weiss and the Pittsburgh Infrastructure Technology Alliance for use of the high-speed camera, and the NanoRobotics Laboratory members for all of their support and suggestions. This work is supported by the National Science Foundation CAREER award program (NSF IIS-0448042) and the NSF Graduate Research Fellowship.

References

Boxerbaum, A., Werk, P., Quinn, D. and Vaidyanathan, R. (2005). Design of an autonomous amphibious robot for surf zone operation. *Proceedings of the IEEE/ASME International Conference on Advanced Intelligent Mechatronics*, pp. 1459–1464.

Bush, J. and Hu, D. (2006). Walking on water: Biolocomotion at the interface. *Annual Review of Fluid Mechanics*, **38**: 339–369.

Crespi, A., Badertscher, A., Guignard, A. and Ijspeert, A. (2005). Amphibot 1: an amphibious snake-like robot. *Robotics and Autonomous Systems*, **50**: 163–175.

Floyd, S., Adilak, S., Rogman, R. and Sitti, M. (2008). Performance of different foot designs for a water running robot. *Proceedings of International Conference on Robotics and Automation*, pp. 244–250.

Floyd, S., Keegan, T. and Sitti, M. (2006). A novel water running robot inspired by basilisk lizards. *Proceedings of the 2006 IEEE/RSJ Int. Conference on Intelligent Robots and Systems*, Beijing, China, pp. 5430–5436.

Floyd, S. and Sitti, M. (2008). Design and development of the lifting and propulsion mechanism for a biologically inspired water runner robot. *IEEE Transactions on Robotics*, **24**(3): 698–709.

Georgiadis, C. (2004). Aqua: An aquatic walking robot. *Proceedings of the IEEE/RSJ International Conference on Intelligent Robots and Systems*, pp. 3525–3531.

Glasheen, J. W. and McMahon, T. A. (1996a). A hydrodynamic model of locomotion in the basilisk lizard. *Nature*, **380**: 340–342.

Glasheen, J. W. and McMahon, T. A. (1996b). Size-dependence of water-running ability in basilisk lizards. *Journal of Experimental Biology*, **199**: 2611–2618.

Guo, S., Fukuda, T. and Asaka, K. (2003). A new type of fish-like underwater microrobot. *IEEE/ASME Transactions on Mechatronics*, **8**: 136–141.

Hu, D., Chan, B. and Bush, J. (2003). The hydrodynamics of water strider locomotion. *Nature*, **424**: 663–666.

Kajita, S., Kanehiro, F., Kaneko, K., Fujiwara, K., Hanada, K., Yokoi, K., Hirukawa, H., Suter, R., Rosenberg, O., Loeb, S., and Long, H. (2003). Biped walking pattern generation by using preview control of zero-moment point. *Proceedings of the IEEE International Conference on Robotics and Automation*, pp. 1620–1626.

Kimura, H., Shimoyama, I. and Miura, H. (1989). Dynamics in the dynamic walk of a quadruped robot. *Advanced Robotics*, **4**(3): 283–301.

Munson, B. R., Young, D. F. and Okiishi, T. H. (2002). *Fundamentals of Fluid Mechanics*. New York, John Wiley and Sons, Inc.

Park, H. S., Floyd, S. and Sitti, M. (2008). Dynamic modeling of a basilisk lizard inspired quadruped robot running on water. *Proceedings of the IEEE/RSJ International Conference on Intelligent Robots and Systems*, pp. 3101–3107.

Park, H. S., Floyd, S. and Sitti, M. (2009). Dynamic modeling and analysis of pitch motion of a basilisk lizard inspired quadruped robot running on water. *Proceedings of the IEEE International Conference on Robotics and Automation*, pp. 2655–2660.

Park, J. and Youm, Y. (2007). General ZMP preview control for biped walking. *Proceedings of the IEEE International Conference on Robotics and Automation*, pp. 2682–2687.

Song, Y., Suhr, S. and Sitti, M. (2006). Modeling of the supporting legs for designing biomimetic water strider robots. *Proceedings of the International Conference on Robotics and Automation*, pp. 2303–2310.

Song, Y. S. and Sitti, M. (2007). Surface tension driven biologically inspired water strider robots: Theory and experiments. *IEEE Transactions on Robotics*, **23**: 578–589.

Suter, R. et al. (1994). Locomotion on the water surface: Propulsive mechanisms of the fisher spider *Dolomedes triton*. *Journal of Experimental Biology*, **200**: 2523–2538.

Takonobu, H., Kodaira, K. and Takeda, H. (2005). Water striders muscle arrangement-based robot. *IEEE/RSJ International Conference on Intelligent Robots and Systems*, pp. 1754–1759.